DOI: 10.1002/hlca.201800227

FULL PAPER

HELVETICA chimica acta

Metal(II) Formates (M = Fe, Co, Ni, and Cu) Stabilized by Tetramethylethylenediamine (tmeda): Convenient Molecular Precursors for the Synthesis of Supported Nanoparticles

Tigran Margossian,[a] Kim Larmier,[a] Florian Allouche,[a] Ka Wing Chan,[a] and Christophe Copéret*[a]

[a] Department of Chemistry and Applied Biosciences, ETH Zurich Vladimir Prelog Weg 1–5, CH-8093 Zurich, Switzerland, e-mail: ccoperet@ethz.ch

γ-Alumina supported 3d transition-metal nanoparticles are commonly used catalysts for several industrial reactions, such as *Fischer-Tropsch*, reforming, methanation, and hydrogenation reactions. However, the activity of such catalyst is often limited by the low metal dispersion and a high content of irreducible metal, inherent to the conventional preparation methods in aqueous phase. In this context, we have recently shown that [{Ni(μ^2-OCHO)(OCHO)(tmeda)}$_2$(μ^2-OH$_2$)] (tmeda = tetramethylethylenediamine) is a suitable molecular precursor for the formation of 1–2 nm large nanoparticles onto alumina. Here, we explore the synthesis of the corresponding Fe, Co, and Cu molecular precursors, namely [{Fe(μ^2-OCHO)(OCHO)(tmeda)}$_4$], [{Co(μ^2-OCHO)(OCHO)(tmeda)}$_2$(μ^2-OH$_2$)], [Cu(κ^2-OCHO)$_2$(tmeda)], which are, like the Ni precursor, soluble in a range of solvents, rendering them convenient metal precursors for the preparation of supported metallic nanoparticles on γ-alumina. Using a specific adsorption of the molecular precursor on γ-alumina in a suitable organic solvent, treatment under H_2 provides small and narrowly distributed Fe (2.5 ± 0.9 nm), Co (3.0 ± 1.2 nm), Ni (1.7 ± 0.5 nm), and Cu (2.1 ± 1.5 nm) nanoparticles. XAS shows that the proportion of MAl_2O_4 (M = Co, Ni, Cu) is small, thus illustrating the advantage of using these tailor-made molecular precursors.

Keywords: Metal formate, tetramethylethylenediamine, specific adsorption, metal(0) nanoparticles.

Introduction

Metal supported nanoparticles are the most common heterogeneous catalysts used in industry.[1–3] They are used in a broad range of applications, such as the methane conversion processes,[4–9] biomass transformation,[10,11] or fine chemical synthesis.[12,13] Numerous parameters influence the performances of these catalysts, such as the type of support,[14,15] the metal nanoparticles size,[16,17] and their interaction with the support.[18–21] Decreasing the size of those supported nanoparticles allows the enhancement of catalyst performances.[7,16,18,22–24] While small particles and good dispersion can be obtained on various supports, a significant fraction of metal can be lost through its incorporation into the support through the formation of hardly reducible metal-aluminum mixed oxides in the case of alumina.[25–27] The reduction of such metal incorporated into the support during the impregnation phase requires the use of high temperature treatment under reductive atmosphere, leading typically to severe sintering of the particles, with nanoparticle size possibly exceeding 10 nm for Cu, Ni, and Co, up to 80 nm for Fe.[23,28–32] Several approaches have been undertaken to avoid these problems, for instance, by modifying conventional preparation methods by either complexing the initial molecular precursor with a chelating ligand,[33–37] or by adding precious metal to the material.[17,38,39] This allows for a drop of the reduction temperature and hence the decrease of particle size. We have recently introduced a Ni formate – [{Ni(μ^2-OCHO)(OCHO)(tmeda)}$_2$(μ^2-OH$_2$)] (**[Ni]**) (tmeda = tetramethylethylenediamine) – as a convenient molecular precursor for the synthesis of 1–2 nm Ni(0) on a broad range of supports through a

Supporting information for this article is available on the WWW under https://doi.org/10.1002/hlca.201800227

specific adsorption method in organic solvent followed by a reduction step under H_2.[7,18] We reasoned that it would be valuable to broaden this approach to other 3d transition metals, namely Fe, Co, and Cu, because of their relatively low cost and use in numerous applications.[40–44] Here, we describe the synthesis of metal formate [{Fe(μ^2-OCHO)(OCHO)(tmeda)}$_4$] (**[Fe]**), [{Co(μ^2-OCHO)(OCHO)(tmeda)}$_2$(μ^2-OH$_2$)] (**[Co]**), and [Cu(η^2-OCHO)$_2$(tmeda)] (**[Cu]**) as precursors for the synthesis of the supported nanoparticles, here using alumina as a prototypical support, commonly used in industry[45–47] that typically suffers from incorporation of the metal ions into its structure, hence the need of high temperature of reduction to generate metal nanoparticles.

Results and Discussion

Fe(II), Co(II), and Cu(II) formate compounds – **[Fe]**, **[Co]**, **[Cu]** – were prepared from readily available metal precursors through the same strategy as previously reported for **[Ni]** using tmeda[7] as a stabilizing ligand (*Scheme 1*). The yields are 34% and 75%, for [{Co(μ^2-OCHO)(OCHO)(tmeda)}$_2$(μ^2-OH$_2$)] (**[Co]**) and [Cu(η^2-OCHO)$_2$(tmeda)]) (**[Cu]**), respectively, while **[Fe]**, a sensitive compound prepared under inert conditions, is obtained in 33% yield. All syntheses can be carried out on a multi-gram scale to give pure crystalline complex soluble in a range of solvent from water to toluene (*Table S1*). While they all display similar structural features, in particular a +2 oxidation state and the presence of octahedral metal sites, they differ by their nuclearity: mono and tetra-nuclear for **[Cu]** and **[Fe]** *versus* dinuclear for **[Co]** as found for the previously reported **[Ni]** complexes. The tmeda ligand is connected in the same η^2 mode for the four different structures. The M_1–N_1(or M_1–N_2) bond distances decrease from 2.295(2) Å for **[Fe]** to 2.192(2) Å for **[Co]**, 2.168(2) Å for **[Ni]**, and 2.028(2) Å for **[Cu]** following the decrease size in metal ionic radius for the Fe^{2+}, Co^{2+}, and Ni^{2+} (*Table 1*).[48] The N_1–M_1–N_2 angle also increases from 80.04(8)° to 87.13(8)° on going from **[Fe]** to **[Cu]**. Overall, their solid-state structure follows the size of the metal: with Fe^{2+}, the larger cation of the series, the compound adopts a tetrameric structure (*Figure 1,a*), while the structures are dimeric or monomeric with smaller M^{2+} ions (M = Co, Ni, and Cu) as shown in *Figure 1,b–1,d*.

Specific adsorption of the different precursors onto dehydroxylated γ-alumina was conducted with an equimolar quantity of precursor with respect to surface –OH (except for **[Fe]**), using toluene for **[Co]** and **[Ni]** *versus* acetonitrile for **[Fe]** and **[Cu]** in order to take into account their specific solubility (*Table S1*). After washing the excess of complex and drying, the metal loading of the different specifically adsorbed precursors was measured by elemental analysis. The metal loading of Fe/Al_2O_3 is 0.82 wt-% for a measured surface area of alumina of 32 $m^2 g^{-1}$, corresponding to 2.9 metal nm^{-2} for Fe/Al_2O_3. As shown in *Figure 2*, the metal loading decreases for the other metals with 2.4 metal nm^{-2} for Co/Al_2O_3, 1.8 metal nm^{-2} for Ni/Al_2O_3 and 1 metal nm^{-2} for Cu/Al_2O_3. It is noteworthy that the precursor loading expressed in number of precursor per nm^2 is similar for all system, close to unity with 0.7 **[Fe]** nm^{-2}, 1.2 **[Co]** nm^{-2}, 0.9 **[Ni]** nm^{-2}, and 1.0 **[Cu]** nm^{-2}, in line with approximately 2 OH nm^{-2} per precursor (*Figure 2*, red columns).[51]

Table 1. Summary of the Bond Distances [Å] from X-ray crystallography of the different complexes.

	[Fe]	[Co]	[Ni]	[Cu]
M^{2+} radius[50]	0.92[a]	0.89[a]	0.83	0.87
M1–O1	2.095(2)	2.075(2)	2.049(2)	2.499(2)
M1–O2	2.171(1)	2.150(1)	2.099(1)	1.992(1)
M1–N1	2.295(2)	2.192(2)	2.168(2)	2.028(2)
M1–N2	2.275(2)	2.207(2)	2.148(2)	2.028(2)

[a]High spin ionic radius, evidenced by UV/Vis for **[Co]** (*Figure 3*).

The structure of the different adsorbed species onto γ-alumina was thus investigated by a combination of spectroscopy methods (IR, UV/Vis, and X-ray absorption spectroscopy (XAS)). The IR spectra of the different specifically adsorbed complexes onto $Al_2O_{3\text{-}500}$ recorded under argon are shown in *Figure S3*. We observe that the specific adsorption of the different precursors induces a shift of the Al–OH bands to lower wavenumbers and to the appearance of C(sp^2)–H, C(sp^3)–H, and C–O bands associated with the formate and tmeda ligands, with bands at 2980 cm^{-1}, 2849 cm^{-1}, 2731 cm^{-1}, 1610 cm^{-1}, and 1470 cm^{-1}. According to XAS, the edge energy decreases from 7120.0 eV for **[Fe]** to 7112.0 eV for Fe/Al_2O_3 (measured from the first inflection point of the spectra), which indicates reduction of Fe centers. However, obtaining information on the coordination environment was not possible due to poor data quality of the extended X-ray absorption fine structure (EXAFS). Linear combination fitting of the Fe/Al_2O_3 XANES spectra shows 45% of **[Fe]** (Fe^{2+}), 34% of Fe_2O_3 (Fe^{3+}), and 21% of Fe foil (Fe^0, *Figure S4*). This complex mixture of Fe species lead us to hypothesize that **[Fe]** partially disproportionate to iron (0) metal and iron oxide (III) upon contact

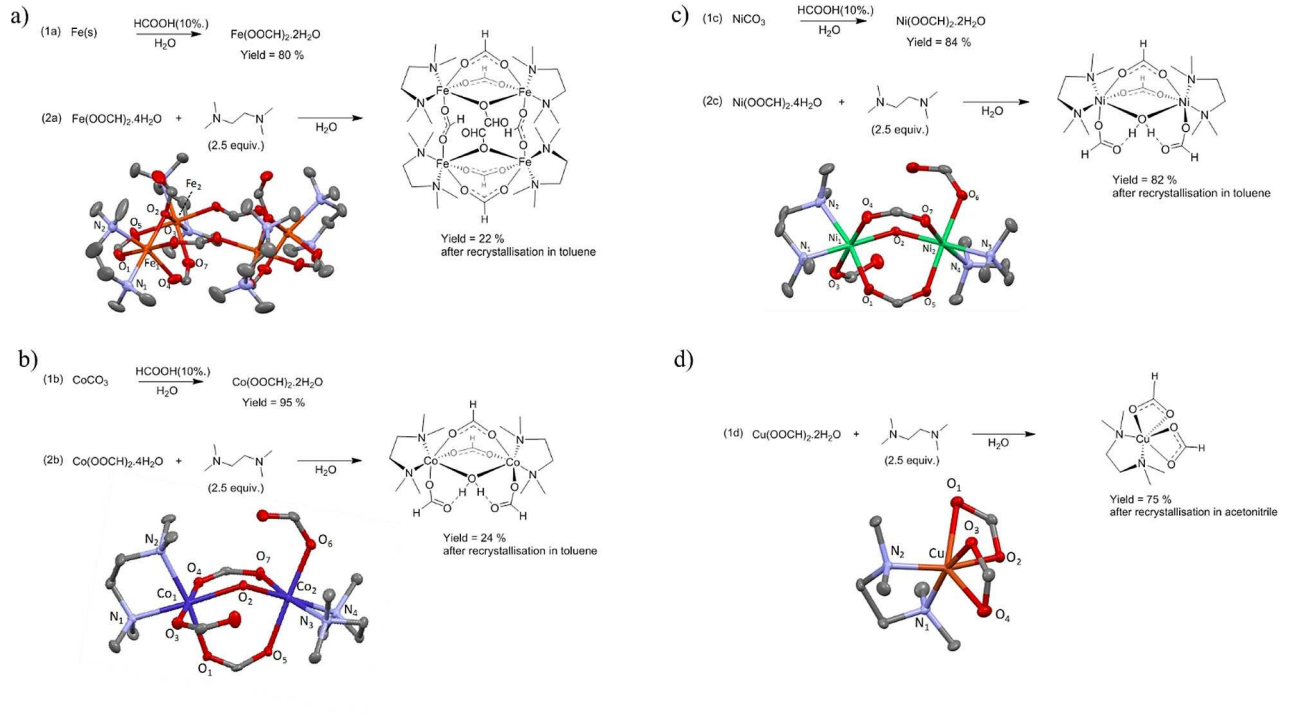

Figure 1. Crystal structure and synthesis path of complex a) **[Fe]**, b) **[Co]**, c) **[Ni]**, and d) **[Cu]**. Thermal ellipsoids were set at 50% probability level and except for μ-H_2O for complex **[Co]** and **[Ni]**, hydrogen atoms and the co-crystallized water molecule are omitted for clarity.[49]

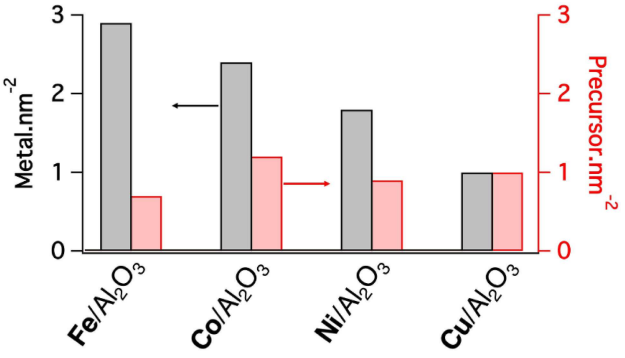

Figure 2. Metal uptake (right column, black) onto $Al_2O_{3\text{-}500}$ and precursor uptake (left column, red) onto $Al_2O_{3\text{-}500}$, which corresponds to the metal loading divided by the number of metal atoms per molecular complex.

onto the alumina surface according to an equation of the type: $3\ Fe^{2+} \rightarrow Fe^0 + 2\ Fe^{3+}$.

The adsorption of **[Co]** onto alumina surface was studied with a similar approach. The UV/Vis spectrum of the **[Co]**-complex shows a unique band at 510 nm that can be assigned to the d-d transition of an octahedral $Co^{2+}(d^7)$.[36] However, Co/Al_2O_3 shows one red-shifted bands at 558 (*Figure 3,a*) by comparison to what is observed for **[Co]**. This is consistent with the coordination of **[Co]** onto the surface hydroxy groups of alumina as previously observed for Ni.[7,25,35] While a change of oxidation state and/or of the geometry could also explain this observation,[36,52] the XANES spectra of **[Co]** and Co/Al_2O_3 (*Figure S5*) show similar edge energies (7719.8 eV and 7720.3 eV, respectively), consistent with the conservation of the Co(II) oxidation state upon dispersion in this case. Furthermore, the absence of a pre-edge feature in both spectra indicates that Co remains octahedral upon adsorption. EXAFS spectra and fits for **[Co]** and Co/Al_2O_3 are shown in *Figure S6*. In the case of the molecular precursor, the fit includes scattering paths of four closest oxygen atoms, two nitrogen atoms, nine carbon atoms from the second sphere, and the other cobalt center. The bond distances obtained from the fit of **[Co]** are consistent with its X-ray structure (*Table S2* and *Table 1*). The best fit of Co/Al_2O_3 is obtained by keeping the octahedral geometry of the initial precursor and by adding one Co–Al scattering path with two aluminum neighbors accounts for two features at 2.86 Å, consistent with a surface coordination complex. A cobalt-cobalt path allows to fit the feature centered at 3.61 Å (*Figures S6–S8*). This sug-

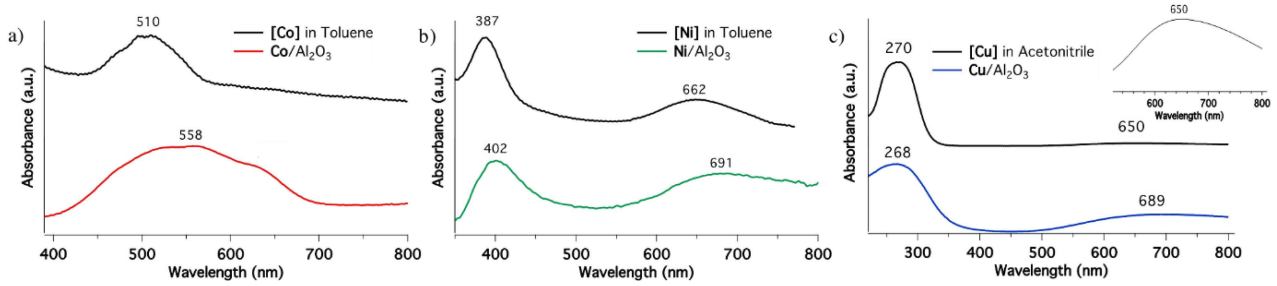

Figure 3. Background subtracted UV/Vis spectra of materials a) Co/Al_2O_3 and **[Co]** in toluene solution, b) Ni/Al_2O_3 and **[Ni]** in toluene solution, c) Cu/Al_2O_3 and **[Cu]** in acetonitrile solution.

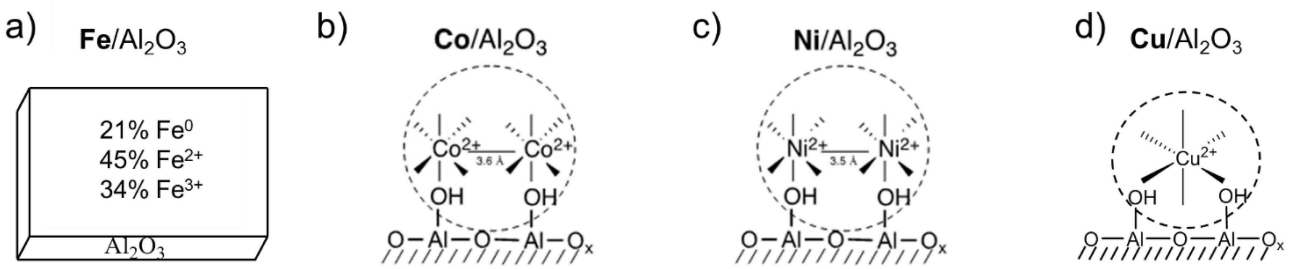

Figure 4. Surface coordination complex for a) Fe/Al_2O_3, b) Co/Al_2O_3, c) Ni/Al_2O_3, and d) Cu/Al_2O_3.

gests that **[Co]** retains its dimeric structure at the surface of alumina (*Figure 4*).

The UV/Vis spectrum of (Cu/Al_2O_3) shares similarities with that of **[Cu]** (*Figure 3,c*), showing bands at 270 nm and 650 nm that can be assigned to charge transfer and d-d of a distorted octahedral $Cu^{2+}(d^9)$.[53] The d-d band of Cu/Al_2O_3 is red-shifted in comparison to the **[Cu]**-complex, which is ascribed to a weaker field ligand environment at the metal such as Al_2O_3.[7,54] Despite the **[Cu]**-complex and Cu/Al_2O_3 cannot be studied by XAS due to the reduction of Cu centers under the X-Ray beam, **[Cu]** likely retains its octahedral structure after adsorption on alumina surface, based on the UV/Vis analysis.

When the different metal formate complexes are specifically adsorbed onto γ-alumina surface, they retain their octahedral conformation for **[Co]** and **[Cu]** as previously observed[7] and re-confirmed for **[Ni]** by UV/Vis spectroscopy (*Figure 3*). In addition, like for Ni, the Co complex retains its dimeric structure upon chemisorption onto γ-alumina surface (*Figure 4,a* and *4,b*).

Following the specific adsorption of the different metal precursor onto the alumina surface, reduction at 700 °C in hydrogen flow yields nanoparticles with particle size distribution of 2.5 ± 0.8 nm for **Fe_{700}** (*Figure 5,a*), 3.0 ± 1.2 nm for **Co_{700}** (*Figure 5,b*), of 1.7 ± 0.5 nm for **Ni_{700}** (*Figure 5,c*), and of 4.5 ± 2.2 nm for **Cu_{700}** (*Figure 5,d*). Smaller and narrower particle size distribution can also be achieved in the case of copper when decreasing the reduction temperature down to 500 °C with an average size of 2.1 ± 1.5 nm (**Cu_{500}**, *Figure S14*).

Depending on the metal precursor specifically adsorbed on the surface, formation and size of the particles are influenced by the reduction temperature and hence, the reducibility of the different systems was estimated by XANES analysis at the respective metal edge after reduction of the samples at 700 °C (*Figure 6*). The XANES spectra of **Co_{700}**, **Ni_{700}**, and **Cu_{700}** (*Figure 6,a*, *6,b*, and *6,c*) are very similar to that of their respective metal foil reference, displaying similar pre-edge and edge positions. In contrast, the XANES spectrum of **Fe_{700}** contains a white line with a normalized adsorption value that is 50% higher than that of the Fe foil reference, indicative of the presence of oxidized iron species. Linear combination fitting of the XANES data for **Fe_{700}** using the Fe foil, $FeAl_2O_4$, and Fe_2O_3 references (*Figure 6,a*) showing that only 40% of total iron was reduced at 700 °C under an H_2 flow. While reducing at 900 °C would likely help to fully reduce the oxidized iron, it has a detrimental effect on particle size, which increases from 2.5 to 7.8 nm. LCF analysis of the XANES data for the three other systems reduced at 700 °C shows that the metal(0) content increases, while moving from left to

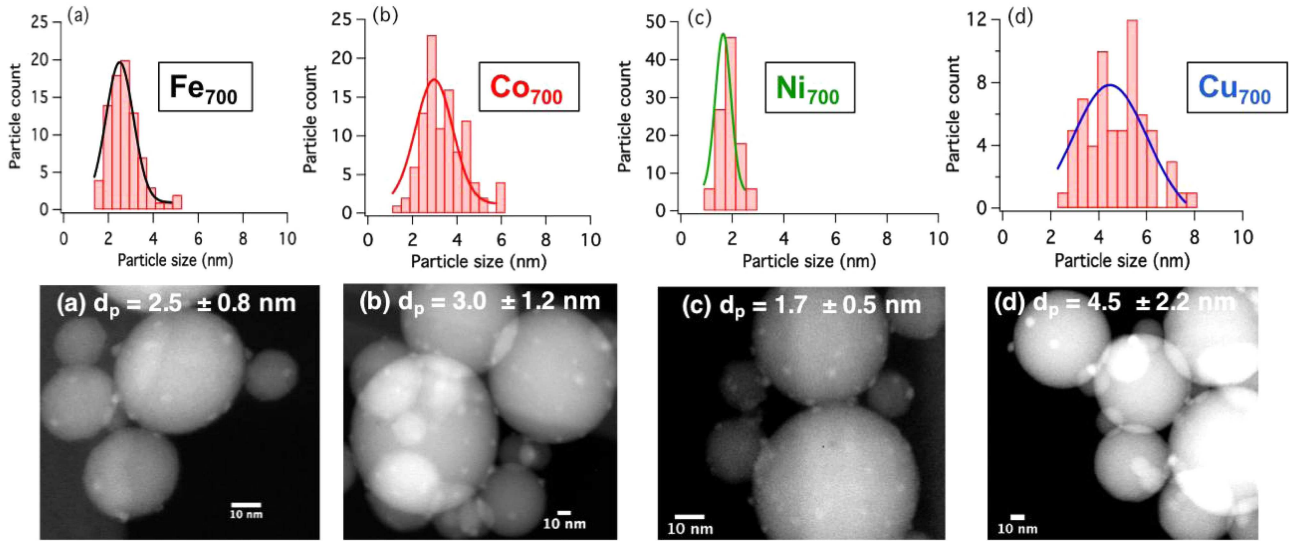

Figure 5. Particle distribution function of the particle size associated to the TEM pictures for the alumina-based catalyst.

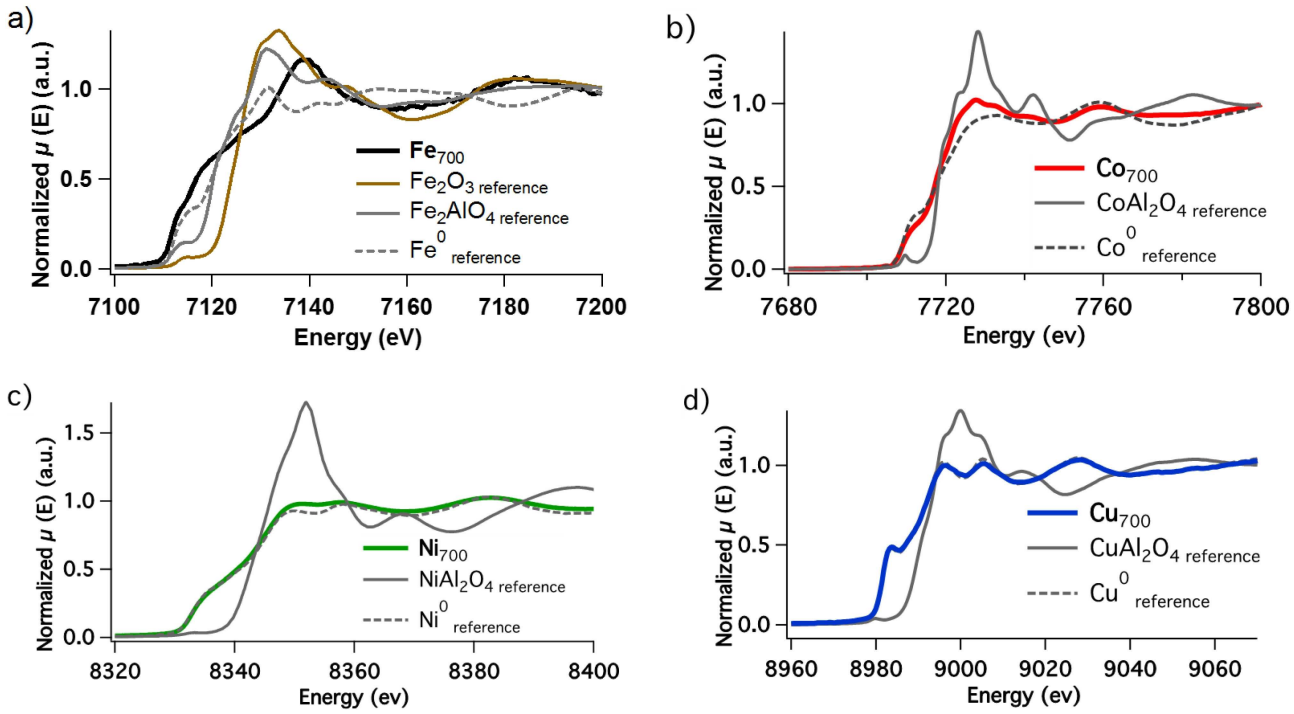

Figure 6. XANES spectrum for the different reduced samples. a) Fe K-edge: **Fe_{700}**, $FeAl_2O_4$, Fe_2O_3, and Fe^0 reference, b) Co K-edge: **Co_{700}**, $CoAl_2O_4$, and Co^0 reference, c) Ni K-edge: **Ni_{700}**, $NiAl_2O_4$, and Ni^0 reference, d) Cu K-edge: **Cu_{700}**, $CuAl_2O_4$, and Cu^0 reference.

right in the periodic table with 80% for **Co_{700}**, 92% for **Ni_{700}**, and 98% for **Cu_{700}**. This is directly in line with the Temperature Programmed Reduction study (*Figure S17*). After reduction at 700 °C, the proportion of fully reduced metal increases from iron to copper (*Figure 7* and *Table 2*).

Conclusions

We have developed the synthesis of 3d metal(II) formate precursors that are convenient for the preparation of small supported nanoparticles using γ-alumina as a prototypical support. The synthesis of the metal formate complexes can be easily carried

out on gram scale. Upon specific adsorption of these different metal(II) complexes onto dehydroxylated alumina, the metal centers retain their coordination environmental (octahedral) and nuclearity, and this approach provides access to high metal loading of approximately one precursor nm^{-2} for all systems. After treatment under hydrogen flow at high temperatures, small and narrowly distributed nanoparticles are formed: iron (2.5 ± 0.8 nm), cobalt (3.0 ± 1.2 nm), nickel (1.7 ± 0.5 nm), and Cu (2.1 ± 1.5 nm), but with their different specificities that follows the reducibility of the metal: 1) the more easily reducible Cu provides Cu(0) nanoparticles at 500 °C, which increases in size upon increasing the temperature of thermal treatment, 2) then Ni provides small Ni(0) particles in a broader range of temperature along with some residual Ni(II) sites, 3) Co follows with an increasing amount of irreducible Co(II) sites, and 4) finally Fe, the more difficult metal to reduce in the series, requires much higher temperature to generate Fe(0) nanoparticles at the expense of suffering from particle sintering.

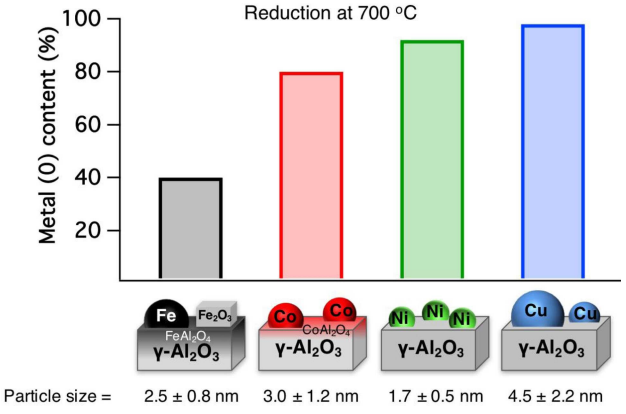

Figure 7. Metal(0) content [%] at 700 °C for the different samples determined from LCF of the XANES spectra at the respective metal edge.

Experimental Section

General Procedure

Iron powder (99%), nickel carbonate (99%), copper formate (99%), and formic acid (99%) were purchased from Sigma-Aldrich and Alfa Aesar. Co and Cu complexes were prepared without particular precautions, while the synthesis of the Fe complex was performed using Schlenk technique due to the sensitivity of $Fe(OCHO)_2 \cdot 2\,H_2O$ towards O_2.[55] De-ionized water was purified using a Purilab instrument (> 10 MΩ cm). Deionized water and formic acid solutions were degassed for 2 h under flow of argon. Extra dry-acetonitrile™ (99.9%) was purchased from Acros. Toluene was purified using double MBraun SPS alumina columns and degassed by argon-bubbling for at least 15 min prior to use. The solvents were stored over molecular sieves. Specific adsorptions were carried out using a Schlenk line with Ar (grade 4.5) and 10^{-3} mbar vacuum.

Support Preparation and Characterization

Alumina nanospheres (NanoSphere) were purchased from Alfa Aesar, NanoDur® with a particle size ranging from 40 nm to 50 nm. The powder XRD pattern shows the presence of a γ-alumina crystalline phase (Figure S2). The BET surface area was estimated at 32 $m^2 g^{-1}$ for NanoSphere material. Prior to use, 6 g of powder was calcined at 500 °C for 12 h (5 °C min^{-1}) under synthetic air flow (100 mL min^{-1}), degassed under high vacuum (10^{-5} mbar) at room temperature for 15 min and stored in a glovebox. As previously

Table 2. Characterization of the as prepared supported nanoparticle catalysts. The alumina supports were dehydroxylated at 500 °C.

Precursor	Solvent	Impregnated material	Reduced material[a]	Metal[b] (wt-%)	Metal density [Metal nm^{-2}]	Particle size[c] [nm]	XANES LCF analysis[d] [%] M(0)	MAl_2O_4
[Fe]	CH_3CN	Fe/Al_2O_3	Fe_{700}	0.82	2.9	2.5 ± 0.9	40	20(40)[e]
[Fe]	CH_3CN	Fe/Al_2O_3	Fe_{900}	0.82	2.9	7.8 ± 3.0	n.d.[f]	n.d.
[Co]	Toluene	Co/Al_2O_3	Co_{700}	0.80	2.4	3.0 ± 1.2	80	20
[Ni]	Toluene	Ni/Al_2O_3	Ni_{700}	0.58	1.8	1.7 ± 0.5	92	8
[Cu]	CH_3CN	Cu/Al_2O_3	Cu_{500}	0.34	1	2.1 ± 1.5	n.d.	n.d.
[Cu]	CH_3CN	Cu/Al_2O_3	Cu_{700}	0.34	1	4.5 ± 2.2	98	2

[a] **Fe_{700}** correspond to Fe/Al_2O_3 reduced at 700 °C. [b] Metal loading determined by elemental analysis. [c] Measured by HAADF/STEM. [d] Determined by Linear Combination Fitting of the XANES spectrum using the corresponding spinel (MAl_2O_4) and foil references; [e] for **Fe_{700}** LCF, an additional Fe_2O_3 reference was used with (value). [f] n.d., not determined.

reported by Wischert et al., Alumina dehydroxylated at 500 °C has a OH surface concentration of 2 per nm^2.[51]

Physisorption of N_2

Nitrogen isotherms at −196 °C were measured on a Bel-Mini apparatus from Bel-Japan. Before measurement, the samples were outgassed under vacuum (ca. 10^{-3} mbar) at 350 °C for 2 h. The BET method[56] was applied to calculate the total surface area.

X-Ray Diffraction (XRD)

The XRD measurements were performed using a Bruker-AXS 'D8 Advance' diffractometer using Cu K_α monochromatic radiation ($\lambda = 1.5418$ Å). The XRD patterns were recorded between 10–80° (2θ with a 0.033° step). The samples were analyzed in the form of a finely crushed powder.

Precursor Complexes Preparation

The [{Ni(μ^2-OCHO)(OCHO)(tmeda)}$_2$(μ^2-OH$_2$)] precursor **[Ni]** was prepared as previously reported.[7]

[{Fe(μ^2-OCHO)(OCHO)(tmeda)}$_4$] ([Fe]). To the iron powder (2 g, 0.036 mol) was added in 85 mL of aqueous formic acid (1.55 mol/L, 0.13 mol). After stirring the mixture under reflux for 2 h, it was filtered to afford a light green solution to which formic acid (5 mL, 0.13 mol) was added. The mixture was taken to dryness under vacuum to afford Fe(OCHO)$_2\cdot$2 H$_2$O (5.25 g, 80 %, 37 mmol).[55] Tetramethylethylenediamine (1.82 mL, 12 mmol) was added to a clear solution of Fe(OCHO)$_2\cdot$2 H$_2$O (1 g, 5.5 mmol) in absolute ethanol (30 mL), leading to a color change to yellow. The mixture was stirred for 5 min, before being taken to dryness. It was extracted with toluene (3×10 mL), concentrated to reach saturation of the solution and crystallized at −38 °C to afford large light yellow crystals of [{Fe(μ^2-OCHO)(OCHO)(tmeda)}$_4$] (0.3 g, 1.2 mmol, yield 22 %) suitable for X-ray crystallography. CCDC-1834512 contains the supplementary crystallographic data. Two successive recrystallization steps in toluene lead to the formation of 0.45 g (yield 33 %, 1.8 mmol). Anal. calc. for $C_{28}H_{68}Fe_4N_8O_{16}$ (996.26): C 33.76, H 6.88, N 11.25; found: C 33.60, H 6.92, N 10.95.

[{Co(μ^2-OCHO)(OCHO)(tmeda)}$_2$(μ^2-OH$_2$)] ([Co]). Formic acid (10 mL, 277 mmol) was added to a solution of Co(CO$_3$) (5.1 g, 43 mmol) in deionized water (100 mL). The mixture was stirred under reflux for 4 h, affording a pink solution. The solution was taken to dryness, treated with absolute ethanol (100 mL), and dried under vacuum (10^{-2} mbar) to yield Co(OCHO)$_2\cdot$2 H$_2$O (7 g, 86 %, 37 mmol).[57] Tetramethylethylenediamine (7.6 mL, 50 mmol) was added to a clear solution of Co(OCHO)$_2\cdot$2 H$_2$O in deionized water (4.0 g, 22 mmol, 100 mL), leading to a pink solution. The mixture turned dark blue while a flocculent precipitate appeared, before finally turning red-brown. The mixture was taken to dryness and extracted with toluene (150 mL). Concentration of the filtrate and crystallization at −38 °C yielded large pink-purple crystals of **[Co]** (1.5 g, yield 24.3 %) suitable for X-ray crystallography. CCDC-1834517 contains the supplementary crystallographic data. Two successive recrystallization steps from toluene lead to the formation of 2.1 g (yield 34 %, 7.5 mmol). Coordinating solvents such as tetrahydrofuran and diethyl ether decoordinates the tetramethylethylenediamine from the metal center. IR (KBr): 3015, 2981, 2888, 2843, 2818, 2800, 2781, 2733, 2697, 1645, 1563, 1465, 1366. Anal. calc. for $C_{16}H_{38}Co_2N_4O_9$ (548.36): C 35.04, H 6.98, N 10.22; found: C 34.95, H 6.73, N 9.93.

[Cu(η^2-OCHO)$_2$(tmeda)] ([Cu]). Tetramethylethylenediamine (1.4 mL, 9.2 mmol) was added to a 30-mL blue solution of Cu(OCHO)$_2\cdot$4 H$_2$O in deionized water (0.98 g, 4.3 mmol), leading to a dark blue solution. The mixture was taken to dryness and extracted with acetonitrile (30 mL). Concentration of the filtrate and crystallization at −38 °C yielded large blue crystals of **[Cu]** (0.85 g, 3.2 mmol, yield 75 %) suitable for X-ray crystallography. CCDC-1834516 contains the supplementary crystallographic data. IR (KBr): 3157, 3019, 3004, 2984, 2929, 2855, 2723, 2616, 1590, 1563, 1461, 1368. Anal. calc. for $C_8H_{18}CuN_2O_4$ (269.78): C 35.62, H 6.72, N 10.38; found: C 35.34, H 6.56, N 10.11.

Specific Adsorption of **[Fe]**, **[Co]**, **[Ni]**, *and* **[Cu]** *onto Alumina*

[{Fe(μ^2-OCHO)(OCHO)(tmeda)}$_4$]/$Al_2O_{3\text{-}500}$ (Fe/Al_2O_3). The compound **[Fe]** (120 mg, 0.12 mmol, 0.3 equiv.) was dissolved in acetonitrile (40 mL) and contacted with 2.0 g of NanoSphere $Al_2O_{3\text{-}500}$ (0.36 mmol AlOH, 1 equiv.). Upon reaction, a gas release was observed in the solution. The mixture was gently stirred for 2 h at room temperature. The solid was washed three times with 20 mL of acetonitrile and dried under vacuum (10^{-5} mbar) for 16 h to yield a white solid. IR: 3510, 3013, 2976, 2876, 2845, 2805, 2735, 1665, 1368.

Elemental analysis: Fe 0.82, C 0.60, H 0.18, N < 0.2, which corresponds to the molar ratio of N/Fe > 1 and C/Fe = 3.4.

[{Co(μ^2-OCHO)(OCHO)(tmeda)}$_2$(μ^2-OH$_2$)]/Al$_2$O$_{3\text{-}500}$ (Co/Al$_2$O$_3$). The compound **[Co]** (172 mg, 0.3 mmol, 0.83 equiv.) was dissolved in toluene (20 mL) and contacted with 2.0 g of NanoSphere Al$_2$O$_{3\text{-}500}$ (0.36 mmol AlOH, 1 equiv.). The mixture was gently stirred for 2 h at room temperature. The solid was washed three times with 20 mL toluene and dried under vacuum (10^{-5} mbar) for 16 h to yield a magenta solid. FT-IR: 3556, 3016, 2980, 2892, 2848, 2732, 1643, 1610, 1470, 1370. Elemental analysis: Co 0.80, C 0.72, H 0.18, N 0.26, with molar ratio of N/Co = 1.4 and C/Co = 4.4.

[{Ni(μ^2-OCHO)(OCHO)(tmeda)}$_2$(μ^2-OH$_2$)]/Al$_2$O$_{3\text{-}500}$ (Ni/Al$_2$O$_3$). The compound **[Ni]** (189 mg, 0.35 mmol, 0.97 equiv.) was dissolved in toluene (20 mL) and contacted with 2.0 g of NanoSphere Al$_2$O$_{3\text{-}500}$ (0.36 mmol AlOH, 1 equiv.). The mixture was gently stirred for 2 h at room temperature. The solid was washed three times with 20 mL of toluene and dried under vacuum (10^{-5} mbar) for 16 h to yield a light green solid. FT-IR: 3669, 3548, 2980, 2881, 2849, 2731, 1662, 1610, 1470, 1394, 1368. Elemental analysis: Ni 0.58, C 0.70, H 0.19, N 0.26, with molar ratio of N/Ni = 1.7 and C/Ni = 5.6.

[Cu(η^2-OCHO)$_2$(tmeda)]/Al$_2$O$_{3\text{-}500}$ (Cu/Al$_2$O$_3$). The compound **[Cu]** (100 mg, 0.38 mmol, 1.05 equiv.) was dissolved in acetonitrile (20 mL) and contacted with 2.0 g NanoSphere of Al$_2$O$_{3-500}$ (0.36 mmol AlOH, 1 equiv.). The mixture was gently stirred for 2 h at room temperature. The solid was washed three times with 20 mL of acetonitrile and dried under vacuum (10^{-5} mbar) for 16 h to yield a light green solid. FT-IR: 3543, 3018, 2979, 2899, 2854,1687, 1636, 1608, 1471. Elemental analysis: Cu 0.36, C 0.43, H 0.18, N < 0.2, with molar ratio of N/Cu < 2 and C/Cu = 6.

Reduction of the Impregnated Materials to Give Supported Nanoparticles

The dried samples were reduced under a flow of pure hydrogen at 500 °C, 700 °C, 900 °C (1 °C min^{-1}) for 8 h. After outgassing under high vacuum (10^{-5} mbar), the catalysts were stored in an Ar atmosphere in a solvent-free glovebox. The code Metal$_{\text{Temperature}}$ refers to the type of metal nanoparticle of the reduced supported nanoparticles and the number in subscript to the reduction temperature.

Scanning Transmission Electron Microscopy (TEM/STEM) *Study*

Prior to TEM analysis, all samples were oxidized by the slow diffusion of air to the catalysts under argon. After oxidation, the materials were dispersed in ethanol and a droplet of the suspension was deposited on a lacey carbon foil supported on a copper grid. Scanning transmission electron microscopy images were recorded on an aberration-corrected Hitachi HD2700CS microscope with a high-angle annular dark field detector (HAADF-STEM). Particle size distribution (PSD) was determined by analyzing 100 nanoparticles and fitting a normal distribution (particle size = mean value ± standard deviation). X-Ray spectra were measured with an energy-dispersive detector (EDX) attached to the HD2700CS. Particle size distributions and EDX spectra are shown in the supplementary information (*Figures S9–S15*). The metal nanoparticles appear bright in the HAADF-STEM images as Ni has the highest atomic number (Z contrast) among the elements present, which was also confirmed by EDX spectroscopy.

UV/Vis Spectroscopy

UV/Visible spectra of the metal salt solutions were recorded with a resolution of 1 nm in the transmission mode on an Agilent Technologies, Cary Series using the corresponding solvent as a reference. UV/Visible spectra of the solids were recorded in the reflectance mode (1-nm resolution) on the same spectrometer, using KBr as a reference. The spectra were collected in an air-free cell which was loaded inside the glovebox. The diffuse reflectance spectra were submitted to the Kubelka-Munk transform.

X-Ray Absorption Spectroscopy (XAS)

XAS experiments were performed at the Swiss-Norwegian Beamlines (SNBL, BM31) at the European Synchrotron Radiation Facility (ESRF). XAS spectra were collected at the Fe, Co, Ni, and Cu K-edges using a double-crystal Si (111) monochromator (continuous scanning in transmission mode). Calibration of the beamline was performed using metal reference foil and MetalAl$_2$O$_4$ reference. XAS transmissions mode spectra were detected using ion chambers filled with He–N$_2$ gas mixtures. Inside the glovebox, 20 mg of

powder sample were pressed into 1 cm ring and sealed into a 4 cm×4 cm aluminum bag. EXAFS data were fitted in R-space (1–3.7 Å) after a Fourier transform (k = 2–10.5 $Å^{-1}$) using a k weight of 1, 2, and 3 for the molecular precursors and the grafted species. XANES spectra of the supported nanoparticles were fitted using a linear combination fitting of Metal foil and $MetalAl_2O_4$ references for cobalt, nickel, and copper-based samples. In the case of iron-based samples, Fe/Al_2O_3 was fitted with **[Fe]**-complex, Fe foil, and Fe_2O_3 references. $\mathbf{Fe_{700}}$ was fitted with Fe foil, FeO, and Fe_2O_3 references.

Temperature-Programmed Reduction (TPR) *Studies*

These experiments were carried out using a BELCAT–B from Bel Japan equipped with a homemade cell allowing the transfer of the sample from the glovebox to the machine without air exposure. Dried sample (100 mg) was introduced into the cell. Prior cell opening to the machine, the entry and outlet tubings were purged with Argon for 30 min using a by-pass system. The TPR decomposition measurement was performed from 25 °C to 900 °C, under 6 % H_2/94 % He using a ramp of 1 °C min^{-1}. The released gas was followed using a calibrated TCD detector and a mass-spectrometer (Bel-Mass).

Single Crystal XRD

The data were collected on a Bruker D8 Venture diffractometer equipped with a CCD area detector using Mo K_α radiation. The crystal was placed in Paratone and mounted in the beam under a flow of nitrogen at 100 K. An empirical absorption correction was performed with SADABS-2008/1 (Bruker). The structure was solved with SHELXL[58] using intrinsic phasing followed by a least-squares refinement (SHELXL-97) using the OLEX 2-1.2 suite of programs.[59] The non-hydrogen atoms were refined anisotropically. The hydrogen atoms were placed at the calculated positions (see the *Supporting Information* file for details).

Acknowledgements

This research was funded by Swiss Innovation Agency Innosuisse and is part of the Swiss Competence Center for Energy Research SCCER Heat and Energy Storage. We are grateful to the European Synchrotron Radiation Facility, Grenoble, France for providing synchrotron radiation beam time at beamline BM31 (31-01-6) of the SNBL and would like to thank Dr. *Wouter Van Beek* for assistance. We thank Dr. *Nikolaos Tsakoumis* for providing reference material for XAS measurements. We thank Dr. *Frank Krumeich* for the STEM measurement and ScopeM (ETH Zürich) for providing measuring time.

Author Contribution Statement

All authors have equally contributed to this work.

References

[1] F. Zaera, 'Nanostructured materials for applications in heterogeneous catalysis', *Chem. Soc. Rev.* **2013**, *42*, 2746–2762.
[2] P. Barbaro, V. Del Santo, F. Liguori, 'Emerging strategies in sustainable fine-chemical synthesis: asymmetric catalysis by metal nanoparticles', *Dalton Trans.* **2010**, *39*, 8391–8402.
[3] A. Roucoux, J. Schulz, H. Patin, 'Reduced Transition Metal Colloids: A Novel Family of Reusable Catalysts?', *Chem. Rev.* **2002**, *102*, 3757–3778.
[4] L. C. Buelens, V. V. Galvita, H. Poelman, C. Detavernier, G. B. Marin, 'Super-dry reforming of methane intensifies CO_2 utilization via Le Chatelier's principle', *Science* **2016**, *354*, 449–452.
[5] B. L. Farrell, V. O. Igenegbai, S. Linic, 'A Viewpoint on Direct Methane Conversion to Ethane and Ethylene Using Oxidative Coupling on Solid Catalysts', *ACS Catal.* **2016**, *6*, 4340–4346.
[6] S. M. Kim, P. M. Abdala, T. Margossian, D. Hosseini, L. Foppa, A. Armutlulu, W. van Beek, A. Comas-Vives, C. Copéret, C. Müller, 'Cooperativity and Dynamics Increase the Performance of NiFe Dry Reforming Catalysts', *J. Am. Chem. Soc.* **2017**, *139*, 1937–1949.
[7] T. Margossian, K. Larmier, S. M. Kim, F. Krumeich, A. Fedorov, P. Chen, C. R. Müller, C. Copéret, 'Molecularly Tailored Nickel Precursor and Support Yield a Stable Methane Dry Reforming Catalyst with Superior Metal Utilization', *J. Am. Chem. Soc.* **2017**, *139*, 6919–6927.
[8] T. Margossian, K. Larmier, S. M. Kim, F. Krumeich, C. Müller, C. Copéret, 'Supported Bimetallic NiFe Nanoparticles through Colloid Synthesis for Improved Dry Reforming Performance', *ACS Catal.* **2017**, *7*, 6942–6948.
[9] P. Wang, G. Zhao, Y. Wang, Y. Lu, '$MnTiO_3$-driven low-temperature oxidative coupling of methane over TiO_2-doped Mn_2O_3-Na_2WO_4/SiO_2 catalyst', *Sci. Adv.* **2017**, *3*, e1603180.
[10] Y. Wang, S. De, N. Yan, 'Rational control of nano-scale metal-catalysts for biomass conversion', *Chem. Commun.* **2016**, *52*, 6210–6224.
[11] P. S. Shuttleworth, M. De bruyn, H. L. Parker, A. J. Hunt, V. L. Budarin, A. S. Matharu, J. H. Clark, 'Applications of nano-

particles in biomass conversion to chemicals and fuels', *Green Chem.* **2014**, *16*, 573–584.
[12] A. Fedorov, H.-J. Liu, H.-K. Lo, C. Copéret, 'Silica-Supported Cu Nanoparticle Catalysts for Alkyne Semihydrogenation: Effect of Ligands on Rates and Selectivity', *J. Am. Chem. Soc.* **2016**, *138*, 16502–16507.
[13] M. Guo, H. Li, Y. Ren, X. Ren, Q. Yang, C. Li, 'Improving Catalytic Hydrogenation Performance of Pd Nanoparticles by Electronic Modulation Using Phosphine Ligands', *ACS Catal.* **2018**, *8*, 6476–6485.
[14] R. C. Reuel, C. H. Bartholomew, 'Effects of support and dispersion on the CO hydrogenation activity/selectivity properties of cobalt', *J. Catal.* **1984**, *85*, 78–88.
[15] M. Shekhar, J. Wang, W.-S. Lee, W. D. Williams, S. M. Kim, E. A. Stach, J. T. Miller, W. N. Delgass, F. H. Ribeiro, 'Size and Support Effects for the Water-Gas Shift Catalysis over Gold Nanoparticles Supported on Model Al_2O_3 and TiO_2', *J. Am. Chem. Soc.* **2012**, *134*, 4700–4708.
[16] G. L. Bezemer, J. H. Bitter, H. P. C. E. Kuipers, H. Oosterbeek, J. E. Holewijn, X. Xu, F. Kapteijn, A. J. van Dillen, K. P. de Jong, 'Cobalt Particle Size Effects in the Fischer-Tropsch Reaction Studied with Carbon Nanofiber Supported Catalysts', *J. Am. Chem. Soc.* **2006**, *128*, 3956–3964.
[17] D. Pakhare, J. Spivey, 'A review of dry (CO_2) reforming of methane over noble metal catalysts', *Chem. Soc. Rev.* **2014**, *43*, 7813–7837.
[18] L. Foppa, T. Margossian, S. M. Kim, C. Müller, C. Copéret, K. Larmier, A. Comas-Vives, 'Contrasting the Role of Ni/Al_2O_3 Interfaces in Water-Gas Shift and Dry Reforming of Methane', *J. Am. Chem. Soc.* **2017**, *139*, 17128–17139.
[19] H. Tang, F. Liu, J. Wei, B. Qiao, K. Zhao, Y. Su, C. Jin, L. Li, J. Liu, J. Wang, T. Zhang, 'Ultrastable Hydroxyapatite/Titanium-Dioxide-Supported Gold Nanocatalyst with Strong Metal-Support Interaction for Carbon Monoxide Oxidation', *Angew. Chem. Int. Ed.* **2016**, *55*, 10606–10611.
[20] D. Gajan, K. Guillois, P. Delichère, J.-M. Basset, J.-P. Candy, V. Caps, C. Coperet, A. Lesage, L. Emsley, 'Gold Nanoparticles Supported on Passivated Silica: Access to an Efficient Aerobic Epoxidation Catalyst and the Intrinsic Oxidation Activity of Gold', *J. Am. Chem. Soc.* **2009**, *131*, 14667–14669.
[21] K. Furman, D. Baudouin, T. Margossian, K. D. Sabnis, Y. Cui, F. H. Ribeiro, C. Copéret, 'Increased methanation activity through passivation of the silica support', *J. Catal.* **2015**, *324*, 9–13.
[22] D. Baudouin, U. Rodemerck, F. Krumeich, A. de Mallmann, K. C. Szeto, H. Ménard, L. Veyre, J.-P. Candy, P. B. Webb, C. Thieuleux, 'Particle size effect in the low temperature reforming of methane by carbon dioxide on silica-supported Ni nanoparticles', *J. Catal.* **2013**, *297*, 27–34.
[23] A. Y. Khodakov, W. Chu, P. Fongarland, 'Advances in the Development of Novel Cobalt Fischer-Tropsch Catalysts for Synthesis of Long-Chain Hydrocarbons and Clean Fuels', *Chem. Rev.* **2007**, *107*, 1692–1744.
[24] K. Murata, Y. Mahara, J. Ohyama, Y. Yamamoto, S. Arai, A. Satsuma, 'The Metal–Support Interaction Concerning the Particle Size Effect of Pd/Al_2O_3 on Methane Combustion', *Angew. Chem. Int. Ed.* **2017**, *56*, 15993–15997.
[25] X. Carrier, J.-B. d'Espinose de la Caillerie, J.-F. Lambert, M. Che, 'The Support as a Chemical Reagent in the Preparation of WO_x/γ-Al_2O_3 Catalysts: Formation and Deposition of Aluminotungstic Heteropolyanions', *J. Am. Chem. Soc.* **1999**, *121*, 3377–3381.
[26] J.-B. d'Espinose de la Caillerie, M. Kermarec, O. Clause, 'Impregnation of γ-Alumina with Ni (II) or Co (II) Ions at Neutral pH: Hydrotalcite-Type Coprecipitate Formation and Characterization', *J. Am. Chem. Soc.* **1995**, *117*, 11471–11481.
[27] J. Abi Aad, P. Courty, D. Decottignies, M. Michau, F. Diehl, X. Carrier, E. Marceau, 'Inhibition by Inorganic Dopants of γ-Alumina Chemical Weathering under Hydrothermal Conditions: Identification of Reactive Sites and their Influence in Fischer-Tropsch Synthesis', *ChemCatChem* **2017**, *9*, 2106–2117.
[28] Y. Chen, D.-L. Peng, D. Lin, X. Luo, 'Preparation and magnetic properties of nickel nanoparticles via the thermal decomposition of nickel organometallic precursor in alkylamines', *Nanotechnology* **2007**, *18*, 505703.
[29] A. Gojova, B. Guo, R. S. Kota, J. C. Rutledge, I. M. Kennedy, A. I. Barakat, 'Induction of Inflammation in Vascular Endothelial Cells by Metal Oxide Nanoparticles: Effect of Particle Composition', *Environ. Health Perspect.* **2007**, *115*, 403.
[30] F. Meshkani, M. Rezaei, 'Simplified direct pyrolysis method for preparation of nanocrystalline iron based catalysts for H_2 purification via high temperature water gas shift reaction', *Chem. Eng. Res. Des.* **2015**, *95*, 288–297.
[31] B. AlSabban, L. Falivene, S. M. Kozlov, A. Aguilar-Tapia, S. Ould-Chikh, J.-L. Hazemann, L. Cavallo, J.-M. Basset, K. Takanabe, 'In-operando elucidation of bimetallic CoNi nanoparticles during high-temperature CH_4/CO_2 reaction', *Appl. Catal. B* **2017**, *213*, 177–189.
[32] J. Schumann, T. Lunkenbein, A. Tarasov, N. Thomas, R. Schlögl, M. Behrens, 'Synthesis and characterisation of a highly active Cu/ZnO:Al Catalyst', *ChemCatChem* **2014**, *6*, 2889–2897.
[33] V. Rodríguez-González, E. Marceau, P. Beaunier, M. Che, C. Train, 'Stabilization of hexagonal close-packed metallic nickel for alumina-supported systems prepared from Ni(II) glycinate', *J. Solid State Chem.* **2007**, *180*, 22–30.
[34] F. Bentaleb, M. Che, A.-C. Dubreuil, C. Thomazeau, E. Marceau, 'Influence of organic additives on the properties of impregnation solutions and on nickel oxide particle size for Ni/Al_2O_3 catalysts', *Catal. Today* **2014**, *235*, 250–255.
[35] F. Negrier, É. Marceau, M. Che, D. de Caro, 'Role of ethylenediamine in the preparation of alumina-supported Ni catalysts from $[Ni(en)_2(H_2O)_2](NO_3)_2$: from solution properties to nickel particles', *C. R. Chim.* **2003**, *6*, 231–240.
[36] F. Dumond, E. Marceau, M. Che, 'A Study of Cobalt Speciation in Co/Al_2O_3 Catalysts Prepared from Solutions of Cobalt-Ethylenediamine Complexes', *J. Phys. Chem. C* **2007**, *111*, 4780–4789.
[37] A. Davantès, C. Schlaup, X. Carrier, M. Rivallan, G. Lefèvre, 'In Situ Cobalt Speciation on γ-Al_2O_3 in the Presence of Carboxylate Ligands in Supported Catalyst Preparation', *J. Phys. Chem. C* **2017**, *121*, 21461–21471.
[38] K. Mori, K. Miyawaki, H. Yamashita, 'Ru and Ru–Ni Nanoparticles on TiO_2 Support as Extremely Active Catalysts for Hydrogen Production from Ammonia-Borane', *ACS Catal.* **2016**, *6*, 3128–3135.
[39] N. E. Tsakoumis, J. C. Walmsley, M. Rønning, W. van Beek, E. Rytter, A. Holmen, 'Evaluation of Reoxidation Thresholds

for γ-Al_2O_3-Supported Cobalt Catalysts under Fischer-Tropsch Synthesis Conditions', *J. Am. Chem. Soc.* **2017**, *139*, 3706–3715.
[40] J.-P. Dacquin, D. Sellam, C. Batiot-Dupeyrat, A. Tougerti, D. Duprez, S. Royer, 'Efficient and Robust Reforming Catalyst in Severe Reaction Conditions by Nanoprecursor Reduction in Confined Space', *ChemSusChem* **2014**, *7*, 631–637.
[41] K. Larmier, W.-C. Liao, S. Tada, E. Lam, R. Verel, A. Bansode, A. Urakawa, A. Comas-Vives, C. Copéret, 'CO_2-to-Methanol Hydrogenation on Zirconia-Supported Copper Nanoparticles: Reaction Intermediates and the Role of the Metal–Support Interface', *Angew. Chem. Int. Ed.* **2017**, *56*, 2318–2323.
[42] S. Tada, K. Larmier, R. Büchel, C. Copéret, 'Methanol synthesis *via* CO_2 hydrogenation over CuO–ZrO_2 prepared by two-nozzle flame spray pyrolysis', *Catal. Sci. Technol.* **2018**, *8*, 2056–2060.
[43] L. Foppa, M.-C. Silaghi, K. Larmier, A. Comas-Vives, 'Intrinsic reactivity of Ni, Pd and Pt surfaces in dry reforming and competitive reactions: Insights from first principles calculations and microkinetic modeling simulations', *J. Catal.* **2016**, *343*, 196–207.
[44] Z. Li, N. M. Schweitzer, A. B. League, V. Bernales, A. W. Peters, A. B. Getsoian, T. C. Wang, J. T. Miller, A. Vjunov, J. L. Fulton, J. A. Lercher, C. J. Cramer, L. Gagliardi, J. T. Hupp, O. K. Farha, 'Sintering-Resistant Single-Site Nickel Catalyst Supported by Metal-Organic Framework', *J. Am. Chem. Soc.* **2016**, *138*, 1977–1982.
[45] K. Wefers, in 'Alumina Chemicals: Science and Technology Handbook', Eds. L. D. Hart, E. Lense, The American Ceramic Society, Westerville, Ohio, 1990, p. 13.
[46] R. K. Oberlander, L. B. Becker, Jr., 'Alumina Dispersion Behavior' Pat. CA000001161331A.
[47] M. Trueba, S. P. Trasatti, 'γ-Alumina as a Support for Catalysts: a Review of Fundamental Aspects', *Eur. J. Inorg. Chem.* **2005**, 3393–3403.
[48] A. M. Bryan, W. A. Merrill, W. M. Reiff, J. C. Fettinger, P. P. Power, 'Synthesis, Structural, and Magnetic Characterization of Linear and Bent Geometry Cobalt(II) and Nickel(II) Amido Complexes: Evidence of Very Large Spin-Orbit Coupling Effects in Rigorously Linear Coordinated Co^{2+}', *Inorg. Chem.* **2012**, *51*, 3366–3373.
[49] A. M. Schmiedekamp, M. D. Ryan, R. J. Deeth, 'Six-Coordinate Co^{2+} with H_2O and NH_3 Ligands: Which Spin State Is More Stable?', *Inorg. Chem.* **2002**, *41*, 5733–5743.
[50] R. D. Shannon, 'Revised effective ionic radii and systematic studies of interatomic distances in halides and chalcogenides', *Acta Crystallogr. Sect. A* **1976**, *32*, 751–767.
[51] R. Wischert, P. Laurent, C. Copéret, F. o. Delbecq, P. Sautet, 'γ-Alumina: the Essential and Unexpected Role of Water for the Structure, Stability, and Reactivity of "Defect" Sites', *J. Am. Chem. Soc.* **2012**, *134*, 14430–14449.
[52] D. P. Estes, G. Siddiqi, F. Allouche, K. V. Kovtunov, O. V. Safonova, A. L. Trigub, I. V. Koptyug, C. Copéret, 'C–H Activation on Co,O Sites: Isolated Surface Sites versus Molecular Analogs', *J. Am. Chem. Soc.* **2016**, *138*, 14987–14997.
[53] A. Lever, 'Electronic spectra of dn ions', in 'Inorganic Electronic Spectroscopy', 2nd Edn., Elsevier, Amsterdam, 1984, pp. 376–611.
[54] L. Bonneviot, O. Legendre, M. Kermarec, D. Olivier, M. Che, 'Characterization by UV-vis-NIR reflectance spectroscopy of the exchange sites of nickel on silica', *J. Colloid Interface Sci.* **1990**, *134*, 534–547.
[55] R. N. Rhoda, A. V. Fraioli, W. L. Taylor, J. Kleinberg, 'Iron(II) Formate', in 'Inorganic Syntheses', Vol. 4, Ed. J. C. Bailar, McGraw-Hill Book Company, Inc., 1953, pp. 159–161.
[56] S. Brunauer, P. H. Emmett, E. Teller, 'Adsorption of Gases in Multimolecular Layers', *J. Am. Chem. Soc.* **1938**, *60*, 309–319.
[57] A. Kaufman, C. Afshar, M. Rossi, D. E. Zacharias, J. P. Glusker, 'Metal ion coordination in cobalt formate dihydrate', *Struct. Chem.* **1993**, *4*, 191–198.
[58] G. M. Sheldrick, 'SHELXT – Integrated space-group and crystal-structure determination', *Acta Crystallogr. Sect. A* **2015**, *71*, 3–8.
[59] O. V. Dolomanov, L. J. Bourhis, R. J. Gildea, J. A. K. Howard, H. Puschmann, '*OLEX2*: a complete structure solution, refinement and analysis program', *J. Appl. Crystallogr.* **2009**, *42*, 339–341.

Received December 4, 2018
Accepted February 5, 2019

